

Derivation of Knockdown Factors for Common Bulkhead Structures Considering Geometric Initial Imperfection and Thermal Transfer Effects

Chang-Min Lee, Chang-Hoon Sim, Gi-Seop Kim, and Jae-Sang Park[†]
Chungnam National University, Department of Aerospace Engineering
99 Deahak-ro Yuseong-gu Deajeon, Republic of Korea

on8915@o.cnu.ac.kr – scc91@cnu.ac.kr – buffon5534607@o.cnu.ac.kr – aerotor@cnu.ac.kr

[†] Corresponding Author

Abstract

The common bulkhead structure can be used to reduce the weight of space launch vehicles. In this study, nonlinear postbuckling analyses are conducted to derive the buckling Knockdown Factor (KDF) for the common bulkhead structures considering geometric initial and thermal imperfection. A commercial finite element analysis program, ABAQUS, is used for modeling and numerical simulations. The Single Perturbation Dimple Approach (SPDA) is used to implement the geometric initial imperfection. The thermal imperfection is represented by thermal–structural coupled analyses. The most conservative KDF in this work is 0.465 when both the geometric initial imperfection and the thermal imperfection are considered. This result is higher by 132% than NASA's buckling design criteria (0.200). Therefore, lightweight design of space launch vehicles may be possible using the present buckling KDFs.

1. Introduction

With the beginning of the new space era, the importance of reducing the weight of space-launch vehicle structures has become apparent [1]. Because the propellant tank structures account for the majority of the weight of launch vehicles, except for the propellant [2], a lightweight design for propellant tank structures is important. As shown in Figure 1 [3], propellant tank structures generally require an interstage to connect the oxidizer and fuel tanks in separate structures, which in turn increases the weight of the propellant tank structures. The common bulkhead structure divides a single-tank structure into oxidizer and fuel regions using a bulkhead, eliminating the need for an interstage [3]. It has been implemented in Space X's Falcon series, ESA's Ariane 5, and Saturn V rockets [4-6]. Therefore, the lightweight design of launch vehicles is possible by using common bulkhead structures to reduce the weight of the propellant tank structures.

The initial imperfections of shell structures that occur during the manufacturing and operation of launch vehicle structures reduce the actual buckling load to a value lower than the theoretical linear buckling load [7]. The buckling Knockdown Factor (KDF, γ) is a design criterion for the shell structures of space launch vehicles that considers the reduction in the buckling load owing to initial imperfections [7]. Buckling KDF is defined in Eq. (1), which is the ratio of the global buckling load considering imperfections ($(N_{cr})_{\text{imperfect}}$) to the global buckling load of the perfect model without imperfections ($(N_{cr})_{\text{perfect}}$).

$$\gamma = \frac{(N_{cr})_{\text{imperfect}}}{(N_{cr})_{\text{perfect}}} \quad (1)$$

The lower the buckling KDF, the heavier and more conservative is the design of the shell structures. Therefore, the buckling KDF is directly related to the lightweight design of launch-vehicle structures. The shell buckling KDFs established by NASA in the 1960s (Figure 2, [8]) for hemispherical shell structures used as common bulkhead structures do not account for the characteristics of modern materials and manufacturing technologies. Therefore, studies were conducted on the buckling behavior of shell structures under external pressure to update previous buckling design criteria [9-15]. A study was conducted to derive a new KDF by implementing a geometric initial imperfection using the Single Perturbation Cutout Approach (SPCA) for shell structures of various shapes [9]. In addition, new buckling design criteria were presented by implementing initial imperfections in shell structures using the Local

Reduced Stiffness Method (LRSM). [10, 11]. Studies investigated that the buckling KDF can be increased by considering the pressure inside a cylindrical shell structure under an axial load [12, 13]. Thus, it was demonstrated that the application of NASA's buckling design criteria to the shell structures of propellant tanks could result in a conservative design. Simulations were performed to investigate the buckling behavior of hemispherical sandwich shell structures with foam cores, which are used as common bulkhead structures in the aerospace industry because of their excellent thermal insulation and specific strength, under external pressure [14, 15]. The validity of the simulations was demonstrated by comparison with experimental results [14, 15]. The heat transfer effects owing to the temperature difference between the oxidizer and fuel should be considered when designing common bulkhead structures. Studies were conducted to investigate the thermal insulation performance of common bulkhead structures [16, 17].

Previous works [9-15] investigated buckling KDFs with various geometric initial imperfections. In addition, studies were conducted on the thermal insulation performance of common bulkhead structures [16, 17]. However, the heat transfer effects of common bulkhead structures can cause structural deformations leading to thermal stress [18]. Therefore, it is necessary to derive the buckling KDF for common bulkhead structures by considering both geometric initial imperfections and heat transfer effects.

In this study, a commercial finite element analysis program, ABAQUS, is used for the modeling and numerical simulations. Thermal-structural coupled analyses and nonlinear post-buckling analyses are performed to investigate the thermal and buckling behaviors and derive the buckling KDFs for common bulkhead structures, considering both heat transfer effects and geometric initial imperfections. The foam core sandwich structure is laminated with thin metal on the top and bottom of the core. Foam core sandwich structures are widely used in the aerospace industry owing to their excellent thermal insulation and strength [19]. Therefore, in this study, hemispherical sandwich-shell structures with foam cores are used to represent the thermal and buckling behaviors of common bulkhead structures. A single perturbation dimple approach (SPDA) is applied to represent the geometric initial imperfections of common bulkhead structures, specifically at the pole of the upper region. The buckling KDFs for hemispherical sandwich common bulkhead structures with foam cores are derived when only geometric initial imperfection or only thermal imperfection are considered, as well as when both factors are considered. The KDFs are then compared with those obtained from NASA SP-8032 [8]. The buckling KDFs in this study show that the buckling KDFs of hemispherical shell structures used as common bulkhead structures may enable the design of lighter space launch vehicle structures than previous NASA buckling KDFs.

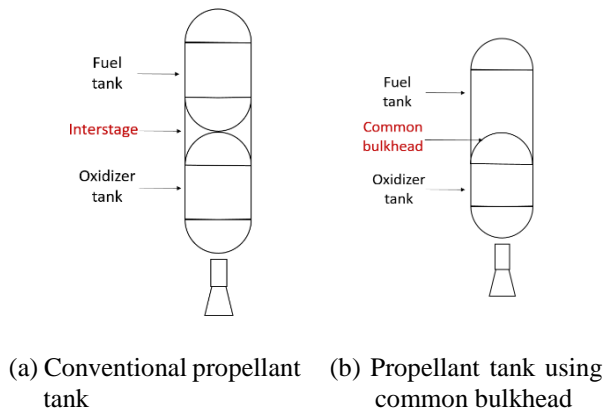


Figure 1: Common bulkhead structures of propellant tank structures for space launch vehicles [3]

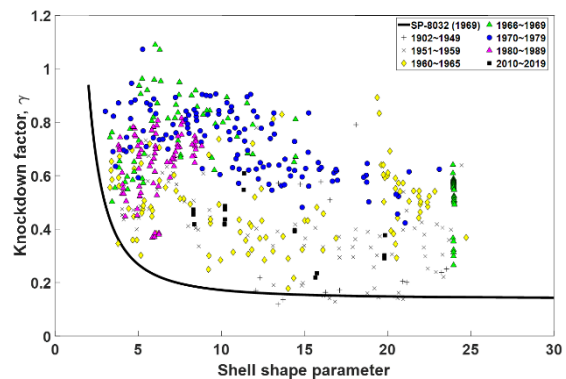


Figure 2: NASA's buckling design criteria and modern buckling knockdown factors [8]

2. Simulation Methods

2.1 Common bulkhead structure models with foam core

The geometric dimensions of a common bulkhead structure [20] are used in this study (Figure 3(a)). AIREX R82.80 [5] and AA2219-T87 [17], are used as the foam core and surface sheet materials, respectively (Table 1, [13]). The common bulkhead structure is simply modeled as a three-dimensional hemispherical shell structure. The upper region of the common bulkhead contains kerosene as fuel for space launch vehicles; however, the lower region contains Liquid Oxygen (LOx) as an oxidizer.

The commercial finite element analysis program ABAQUS, is used for finite element modeling and numerical analyses in this study. Figure 3(b) shows the finite element model for the common bulkhead structures and boundary

conditions. For finite element modeling of thermal-structural coupled analyses, coupled temperature-displacement elements for two-dimensional (2D) shell (S4RT) and three-dimensional (3D) solid (C3D8RT) elements are applied to the surface sheet and foam core, respectively; however, for finite element modeling of nonlinear post-buckling analyses, 2D shell (S4R) and 3D solid (C3D8R) elements are used. Solid elements (C3D8R) are used to model the foam core to account for the large deformation caused by the significant volume change. The finite element sizes of the foam core and surface sheet are determined from the convergence tests to be 0.026 and 0.025 m, respectively. The ‘Tie’ constraint method is applied to couple the finite elements of surface sheets (S4R and S4RT) and foam core (C3D8R and C3D8RT).

Table 1: Properties for hemispherical sandwich common bulkhead structures with foam core

	Foam core	Surface sheet
Conductivity [W/m·°C]	0.037	121
Specific heat [J/kg·°C]	625	864
Density [kg/m ³]	80	2840
Expansion [°C ⁻¹]	4×10 ⁻⁵	2.200×10 ⁻⁵
Elastic modulus [MPa]	42.100	73.100×10 ³
Initial temperature [°C]	15	15
Poisson's ratio	0	0.330

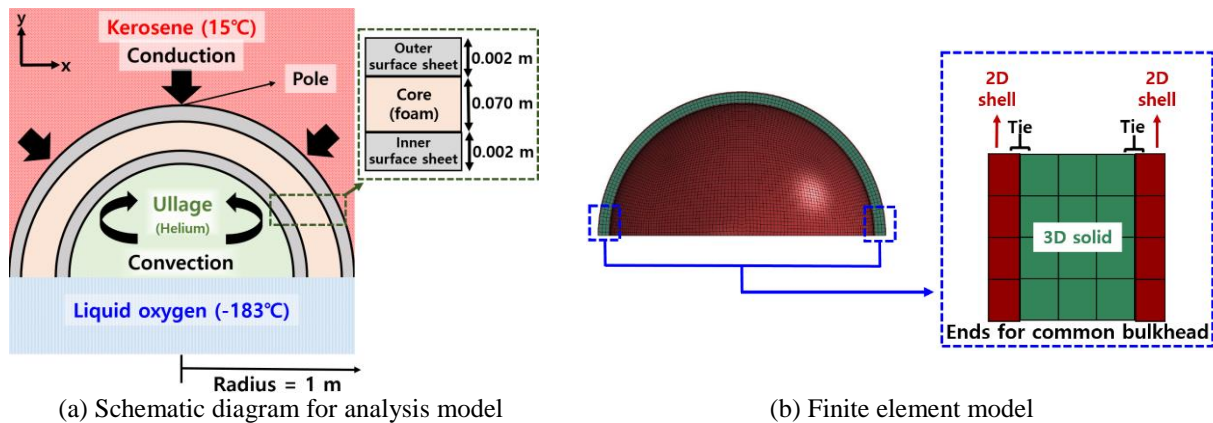


Figure 3: Finite element analysis model for the common bulkhead structures with foam core

2.2 Material nonlinearity modeling techniques

Material nonlinearity modeling is important for representing the structural behavior of foam core sandwich structures [21]. First, the plasticity of metallic material AA2219-T87 is considered. Figure 4 shows the true stress-strain curve of the AA2219-T87 material [22] to represent plasticity. Secondly, the nonlinear compressive behavior of the soft foam core should be considered because the foam core exhibits large deformations with significant volume changes. The plastic deformation of the foam core material is caused by hydrostatic pressure owing to its porous properties. Furthermore, foam hardening occurs via densification when the foam is significantly deformed [23]. In this study, the crushable foam modeling technique provided in ABAQUS is used to simulate the nonlinear compressive behavior of the foam core material [24]. The compression yield stress ratio (K) and hydrostatic yield stress ratio (K_t) derived from the yield surface of the foam core material are required for crushable foam modeling. The yield surface of the foam core material is defined by the hydrostatic pressure (p) and von Mises stress (q), which are determined through hydrostatic tests. However, to simplify complex hydrostatic tests, a previous study [25] used different methods to define the yield surface of the foam core material. In the study, the yield strength values (σ_c , σ_t , and τ) obtained from the uniaxial compression test, uniaxial tension test, and shear test, respectively, were used to define the yield surface. In the present paper, based on the reference [24], Eq. (2), calculates p and q , which are the three points on the yield

surface [25]. The values of σ_c , σ_t , and τ for AIREX R82.80 are 1.13 MPa [26], 1.28 MPa [27], and 1.10 MPa [28], respectively. Using the values of p and q , Eq. (3) defines the yield surface [25], and Eq. (4) [25] derives the values of $K=2.37$ and $K_t=1.17$, which are used in the crushable foam modeling. The foam hardening data for the crushable foam represent the densification of the foam core material. Figure 5 shows the yield surface (Eq. (3)) and foam hardening data [26] for crushable foam modeling in this study. A further detailed explanation of the crushable foam modeling can be found in reference [25].

$$\begin{aligned} p &= -\sigma_c/3, q = \sigma_c \text{ (uniaxial compression test)} \\ p &= -\sigma_t/3, q = \sigma_t \text{ (uniaxial tension test)} \\ p &= 0, q = \sqrt{3}\tau \text{ (shear test)} \end{aligned} \quad (2)$$

$$\frac{(p - (p_c - p_t)/2)^2}{((p_c + p_t)/2)^2} + \frac{q^2}{((3K/\sqrt{(3K_t + K)(3 - K)})(p_c + p_t)/2)^2} = 1 \quad (3)$$

$$\text{where } K = \sigma_c/p_c, K_t = p_t/p_c \quad (4)$$

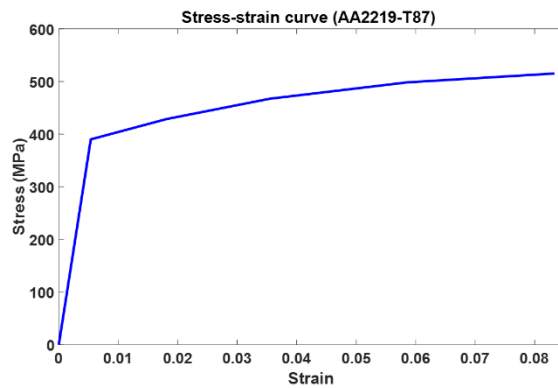


Figure 4: True stress-strain curve for surface sheet using AA2219-T87 [22]

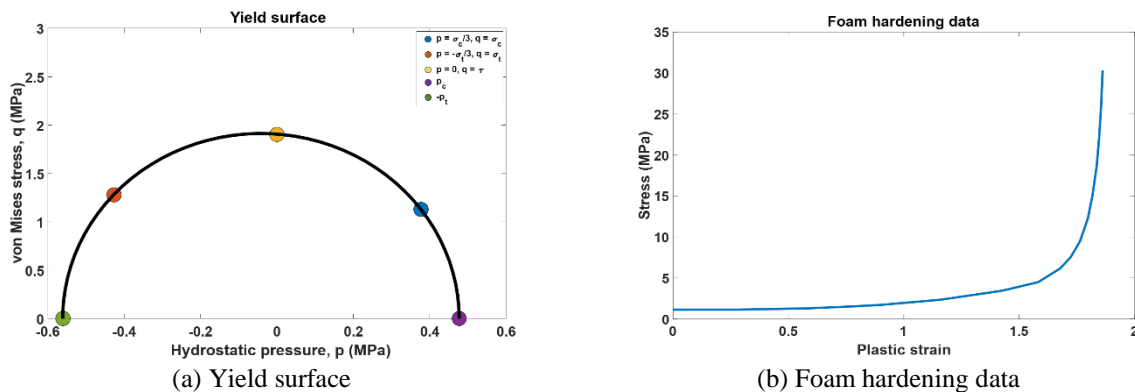


Figure 5: Input data for the crushable foam modeling for the foam core using AIREX R82.80

2.3 Imperfection modeling techniques

2.3.1 Imperfection modeling: Geometric initial imperfection

A realistic geometric initial imperfection for a thin-walled shell structure is represented using a dimple shape, which reduced the buckling load of the thin-walled structure [29, 30]. Similar to the Single Perturbation Load Approach (SPLA), the dimple imperfection for the thin-walled shell structure may be numerically implemented by applying concentrated force to the specific location of a hemispherical shell structure. The geometric initial imperfection by the SPLA at the pole significantly decreased the buckling load of spherical shell structures [31]. However, the large localized deformation of the foam is caused by the enforced concentrated force since the foam in the present study is modeled using 3D solid elements, which may result in poor mesh quality, leading to inaccurate numerical analysis results.

Therefore, this study uses the single perturbation dimple approach (SPDA) to model the geometric initial imperfection of the common bulkhead structure. Figure 6(a) shows a schematic diagram of the SPDA. The radius of the analytical rigid shell is assumed as 10% of the common bulkhead radius [32]. The enforced displacement in the transverse direction is applied to the reference point of the analytical rigid shell. A surface-to-surface contact method is applied to model the contact between the analytical rigid shell and common bulkhead structures. As shown in Figure 6(b), a single dimple is generated at the pole of the common bulkhead structure. The quasi-static analysis technique in ABAQUS/Implicit is used to calculate the geometric initial imperfection when the enforced transverse displacement is applied to a analytical rigid shell. The geometric initial imperfection by SPDA is denoted as ‘Imperfection_{SPDA}’ in this study.

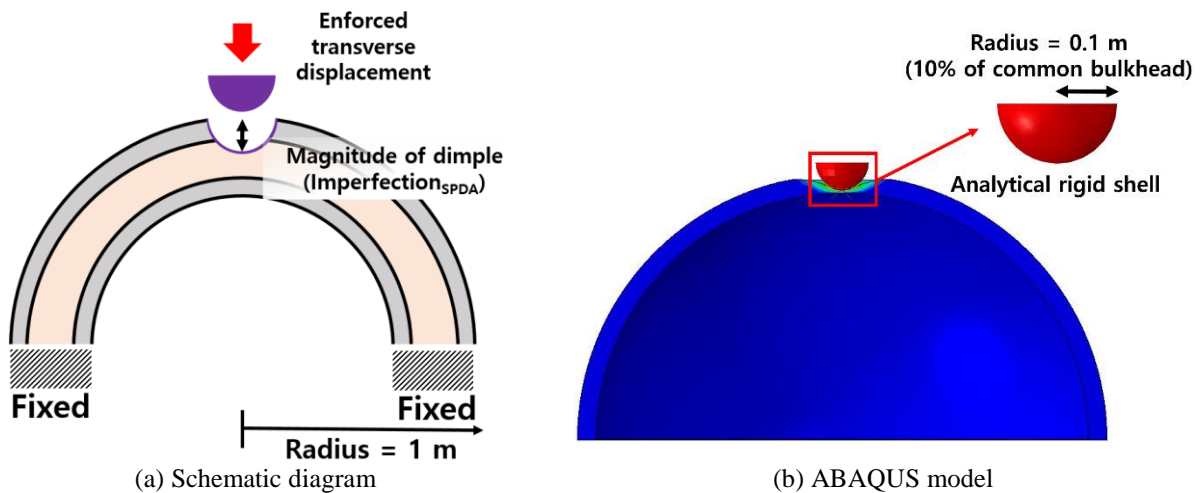


Figure 6: Single Perturbation Dimple Approach (SPDA) for the geometric initial imperfection of common bulkhead structures

2.3.2 Imperfection modeling: Thermal imperfection

The temperature difference between the fuel and the oxidizer causes thermal deformation of the common bulkhead structure, and these deformations can be considered as one of the imperfections. Therefore, it is necessary to study the buckling behavior of common bulkhead structures by considering the imperfections caused by heat transfer effects. As shown in Figure 3(a), it is assumed that heat conduction occurs in the upper region of common bulkhead structures; however, heat convection occurs between the LOx and Ullage with Helium in the lower region. The heat convection coefficient is 10 W/m²·°C [15]. The initial temperature for the common bulkhead structures is 15°C. Transient thermal-structural coupled analyses for the perfect model without any imperfections are conducted using the coupled temperature-displacement method in ABAQUS to calculate the thermal stresses and deformations. The total simulation period in this study is 150 s, which is the combustion time of the first-stage propellant tank of the Korea Space Launch Vehicle-II (KSLV-II) [33]. Figure 7 shows a schematic of the thermal-structural coupled analysis. The imperfection by heat transfer effects only is defined as ‘Imperfection_{thermal}’ in the present work.

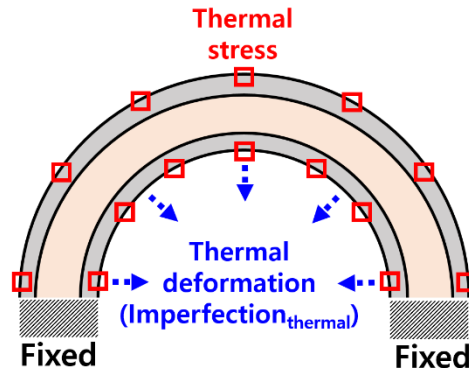


Figure 7: Thermal stresses and deformations represented by thermal effects

2.4 Nonlinear postbuckling analyses with imperfections

Nonlinear postbuckling analyses are performed to investigate the global buckling loads and postbuckling behaviors of common bulkhead structures with and without imperfections when an external pressure is applied. This study uses the quasi-static analysis technique in ABAQUS/Implicit, which converts the static energy released from the buckling behavior with large deformations into kinetic energy. This technique may improve the numerical stability of nonlinear calculations. When the kinetic energy increases rapidly, global buckling occurs, and the postbuckling behavior is investigated up to a ratio of 10% of the kinetic energy to the internal energy. The ratio should not exceed 10% for reliable numerical results of the quasi-static analysis [34]. The postbuckling analyses under external pressures are conducted using the following procedures when the geometric initial imperfection described in Section 2.3.1, the thermal imperfection only explained in Section 2.3.2 is applied, or both are implemented.

2.4.1 Geometric initial imperfection only

The nondimensional imperfection magnitude, μ , (Eq. (5)) is used when the nonlinear postbuckling analyses are conducted with different geometric initial imperfection magnitudes. As the magnitude of μ increases, the global buckling load decreases and converges to the constant value at a certain magnitude of μ . Figure 8(a) shows a schematic of the nonlinear postbuckling analyses for the common bulkhead with Imperfection_{SPDA} when the geometric initial imperfection only is considered. The procedures for nonlinear postbuckling analysis considering the Imperfections_{SPDA} are summarized in Figure 8(b) and explained as follows.

1) The deformed common bulkhead model by SPDA with the prescribed value of μ is used for the nonlinear postbuckling analyses. As described in Section 2.3.1, this deformed configuration represents a common bulkhead structure with a geometric initial imperfection (Imperfection_{SPDA}). Because no external forces are applied in this step, the deformed model is in a stress-free state.

2) The external pressure for nonlinear postbuckling analyses is applied to deformed common bulkhead structures. The global buckling load (or global buckling pressure) and postbuckling behavior are investigated in this step.

3) The analyses in Steps 1) and 2) are repeated until the global buckling pressure converges as the magnitude of μ increases. The global buckling pressure does not decrease and remains constant when μ exceeds a certain value ($\mu_{\text{converged}}$). The buckling KDFs are obtained from using Eqs. (1) using the converged global buckling pressure ($(N_{cr})_{\text{imperfect}}$) and the global buckling pressure of the perfect model without any imperfections ($(N_{cr})_{\text{perfect}}$). In this section, the buckling KDF is calculated by considering only the geometric initial imperfections implemented by the SPDA.

$$\mu = \frac{\text{Magnitude of dimple (Imperfection}_{\text{SPDA}})}{\text{Thickness of common bulkhead}} \quad (5)$$

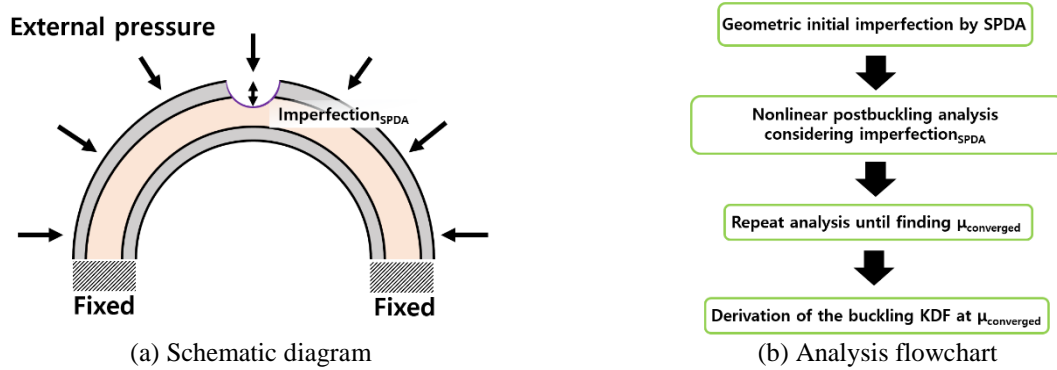


Figure 8: Postbuckling analysis considering the geometric initial imperfection only

2.4.2 Thermal imperfection only

Figure 9(a) shows a schematic diagram of the nonlinear postbuckling analyses for a common bulkhead with thermal imperfection only owing to heat transfer effects ($\text{Imperfection}_{\text{thermal}}$). The procedures for the nonlinear postbuckling analysis considering $\text{Imperfection}_{\text{thermal}}$ are summarized as follows (Figure 9(b)).

1) A transient thermal-structural coupled analysis is performed to calculate the thermal stresses and deformations owing to the heat transfer effects for the common bulkhead structure. In this step, a deformed configuration model with $\text{Imperfection}_{\text{thermal}}$ is obtained and used in the next step.

2) A nonlinear postbuckling analysis for the deformed common bulkhead model obtained from the previous step is performed when an external pressure is applied. It is noteworthy that $\text{Imperfection}_{\text{thermal}}$ is implemented only, without $\text{Imperfection}_{\text{SPDA}}$ and pre-thermal stresses are considered. The global buckling pressure and post-buckling behavior are investigated in this step.

3) The buckling KDF considering only thermal imperfection is derived using Eq. (1), using the global buckling pressure ($(N_{\text{cr}})_{\text{imperfect}}$) calculated in Step 2) and the global buckling pressure of the perfect model without any imperfections ($(N_{\text{cr}})_{\text{perfect}}$).

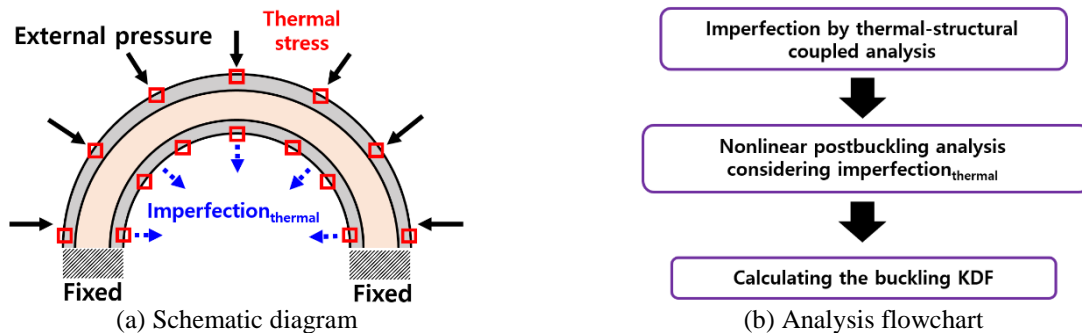


Figure 9: Postbuckling analysis considering the thermal imperfection only

2.4.3 Both geometric initial imperfection and thermal imperfection

As shown in Figure 10(a), postbuckling analyses under external pressure are performed when both geometric initial imperfection ($\text{Imperfection}_{\text{SPDA}}$) and thermal imperfection ($\text{Imperfection}_{\text{thermal}}$) are applied to the common bulkhead structure. In this case, the analysis procedures in Section 2.4.1 and 2.4.2 are used together to investigate the buckling behavior of common bulkhead structures. The processes for nonlinear postbuckling analysis considering both $\text{Imperfection}_{\text{SPDA}}$ and $\text{Imperfection}_{\text{thermal}}$ are shown in Figure 10(b).

1) The thermal-structural coupled analysis explained in Section 2.4.2 is conducted for the deformed common bulkhead structure at $\mu_{\text{converged}}$ obtained in Section 2.4.1. Therefore, a deformed configuration with both $\text{Imperfection}_{\text{SPDA}}$ and $\text{Imperfection}_{\text{thermal}}$ is obtained in this step. This deformed model is used in the next step.

2) A nonlinear post-buckling analysis under external pressure is performed for a deformed common bulkhead structure with both geometric initial imperfection and thermal imperfection. In this step, the global buckling pressure and postbuckling behavior of common bulkhead structures are investigated.

3) The buckling KDF is derived using Eq. (1), using the global buckling pressure considering both the geometric initial imperfection and thermal imperfection ($(N_{cr})_{\text{imperfect}}$) and the global buckling pressure of the perfect model without any imperfections ($(N_{cr})_{\text{perfect}}$).

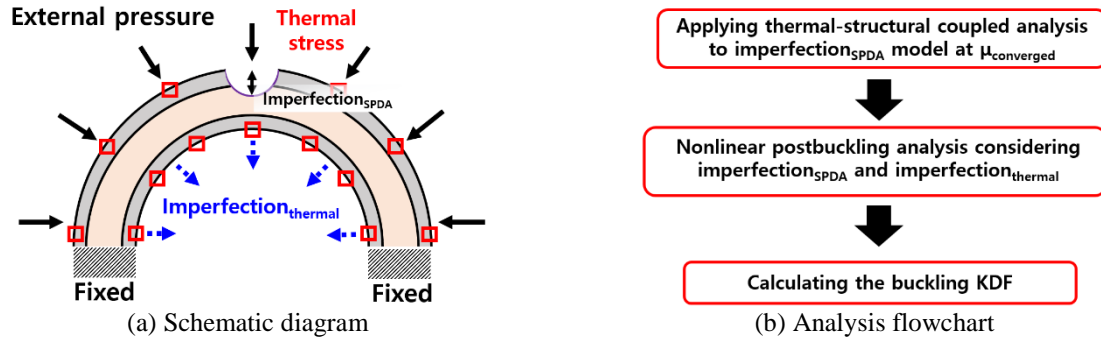


Figure 10: Postbuckling analysis considering both the geometric initial imperfection and the thermal imperfection

3. Numerical Results and Discussion

3.1 Perfect model without any imperfections

Figure 11 shows the results of the buckling analyses for the perfect model of common bulkhead structures without any imperfections. The global buckling pressure for the perfect model without any imperfections is calculated to be 2.152 MPa, which is obtained from linear buckling analysis. However, the global buckling pressure from the nonlinear buckling analysis is predicted to be 1.782 MPa, which is 17% lower than the linear buckling pressure. Because the linear buckling load is generally similar to the nonlinear buckling load for thin-walled shell structures, the geometric nonlinearity is not significant for the global buckling load; thus, the difference in the global buckling loads between the linear buckling and postbuckling analyses in this study may be due to material nonlinearity, including plasticity. Nevertheless, the difference in buckling pressure caused by material nonlinearity is difficult to predict in the preliminary design of common bulkhead structures. Therefore, the linear buckling pressure of the perfect model (2.152 MPa, $(N_{cr})_{\text{perfect}}$) is used to derive the buckling KDFs (Eq. (1)): In addition, buckling waves in the linear analysis are observed in the upper region of common bulkhead structures; however, buckling waves in the nonlinear analysis are generated near fixed boundary conditions.

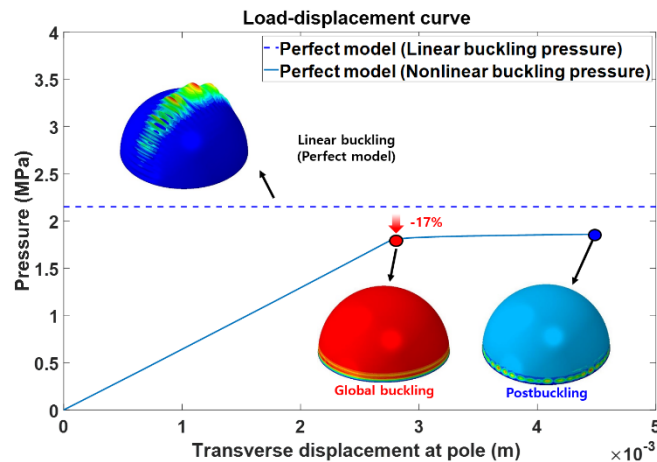


Figure 11: Postbuckling analysis results for the perfect common bulkhead structure models without any imperfections

3.2 Geometric initial imperfection only

The buckling behaviors are investigated for the common bulkhead structure with geometric initial imperfection ($\text{Imperfection}_{\text{SPDA}}$) only, which is modeled using SPDA. Figure 12 shows the convergence of the global buckling pressure. The global buckling pressure (1.101 MPa, $(N_{\text{cr}})_{\text{imperfect}}$) is calculated from the nonlinear postbuckling analyses considering $\text{Imperfection}_{\text{SPDA}}$ when the nondimensional imperfection magnitude is 0.7 ($\mu_{\text{converged}}=0.7$). The deformed configuration at $\mu_{\text{converged}}$ is given in Figure 13. $(N_{\text{cr}})_{\text{imperfect}}$ is 49% lower than $(N_{\text{cr}})_{\text{perfect}}$. Figure 14(a) shows the load-displacement curve of the nonlinear postbuckling analyses for the common bulkhead structures under external pressure with $\text{Imperfection}_{\text{SPDA}}$ at $\mu_{\text{converged}}$. Owing to the geometric initial imperfection, the load-displacement curve is shifted by 0.052 m (70% of the thickness of the common bulkhead). As shown in Figure 14(b), global buckling (A) is observed near the pole, where the geometric initial imperfection is modeled using SPDA. The dimple shape spread out from the pole in all directions when post-buckling (B) occurs. Figure 15 compares the present buckling KDF considering the geometric initial imperfection only (0.512) with that of NASA SP-8032 (0.200). The buckling KDF in this section is 156% higher than that of the NASA buckling design criteria.

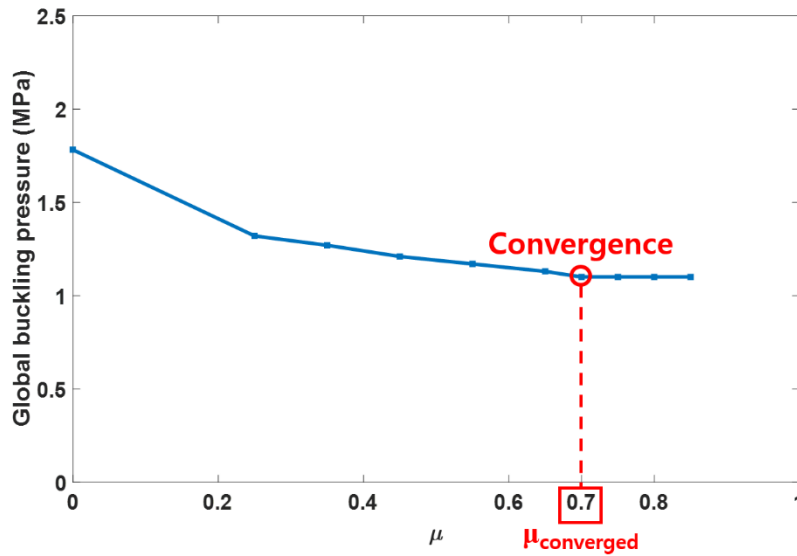


Figure 12: Convergence for the global buckling pressure in terms of nondimensional geometric initial imperfection magnitude μ

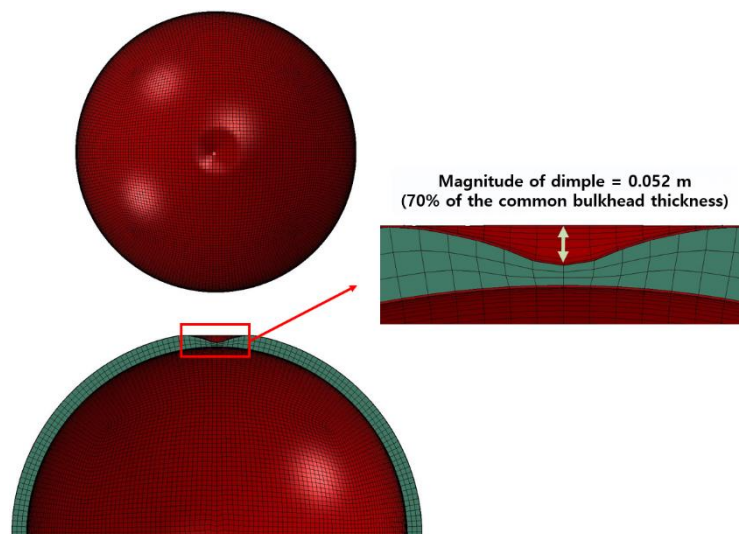


Figure 13: The deformed common bulkhead structures caused by SPDA at $\mu_{\text{converged}}=0.7$

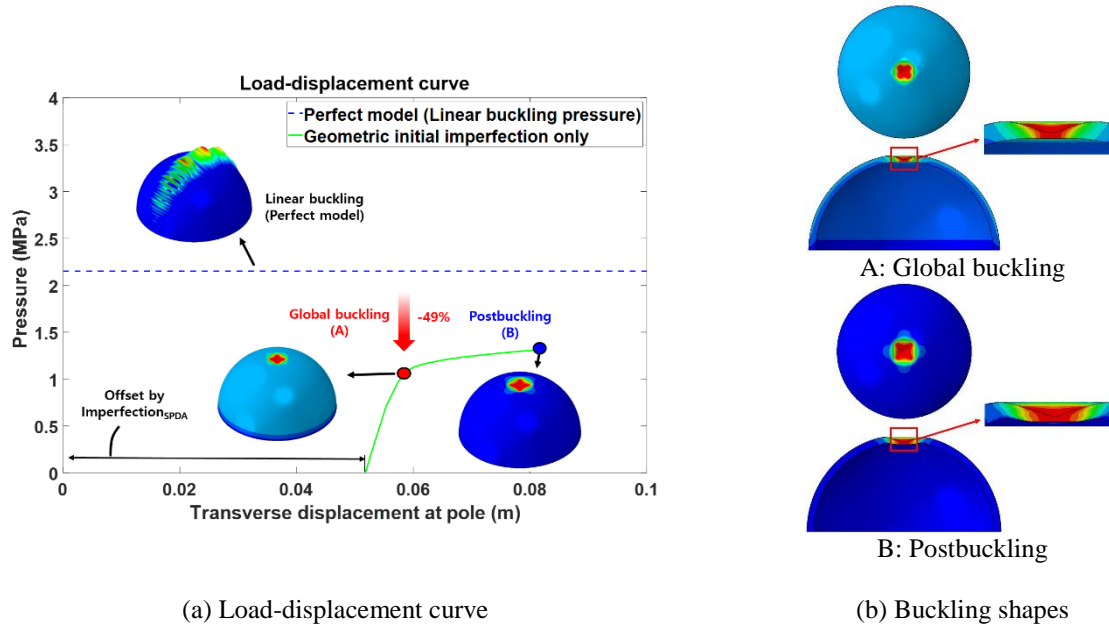


Figure 14: Postbuckling analysis results for the common bulkhead structure considering geometric initial imperfection only

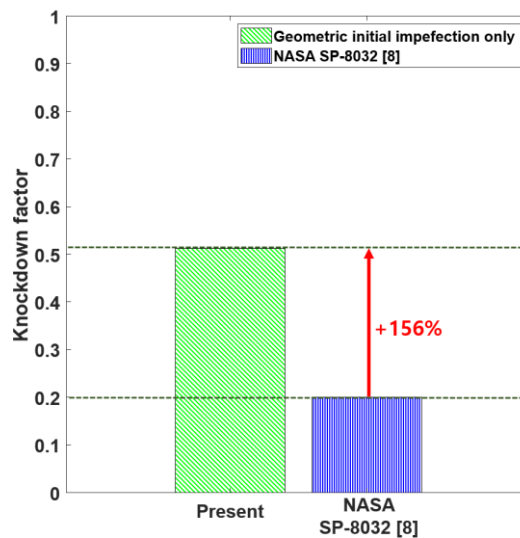


Figure 15: Comparison the buckling KDFs between the common bulkhead structure with geometric initial imperfection only and NASA's buckling design criteria [8]

3.3 Thermal imperfection only

In this section, nonlinear postbuckling analyses are conducted for a common bulkhead structure considering only thermal imperfection. Figure 16 illustrates the transient thermal-structural coupled analysis results for a perfect model without any imperfections. The temperature, displacement, and stress fields of the common bulkhead structures are investigated. The temperature of the lower region decreases 15°C to -42°C due to the heat convection between Ullage and Lox, which shrinks the common bulkhead structure. The deformed configurations represent the common bulkhead structure with the thermal imperfection ($\text{Imperfection}_{\text{thermal}}$).

Figure 17 shows the nonlinear postbuckling analyses under external pressure when thermal imperfection is applied. The load-displacement curve is shifted by 0.158×10^{-3} m owing to thermal imperfection (Figure 17(a)). This result indicates that the deformed configuration caused by $\text{Imperfection}_{\text{thermal}}$ is much smaller than that created by the $\text{Imperfection}_{\text{SPDA}}$ in the previous section. The global buckling pressure with $\text{Imperfection}_{\text{thermal}}$ ($(N_{\text{cr}})_{\text{imperfect}}$) is predicted

to be 1.641 MPa, which is 24% lower than that of $(N_{cr})_{perfect}$. Figure 17(b) shows the global buckling and post-buckling shapes. Global buckling waves(A) are shown adjacent to fixed boundary conditions. After global buckling, the buckling waves deepened in the transverse direction, and post-buckling (B) is observed. As shown in Figure 18, the buckling KDF (0.763) derived in this section is 281% higher than that of NASA's buckling design criteria (0.200).

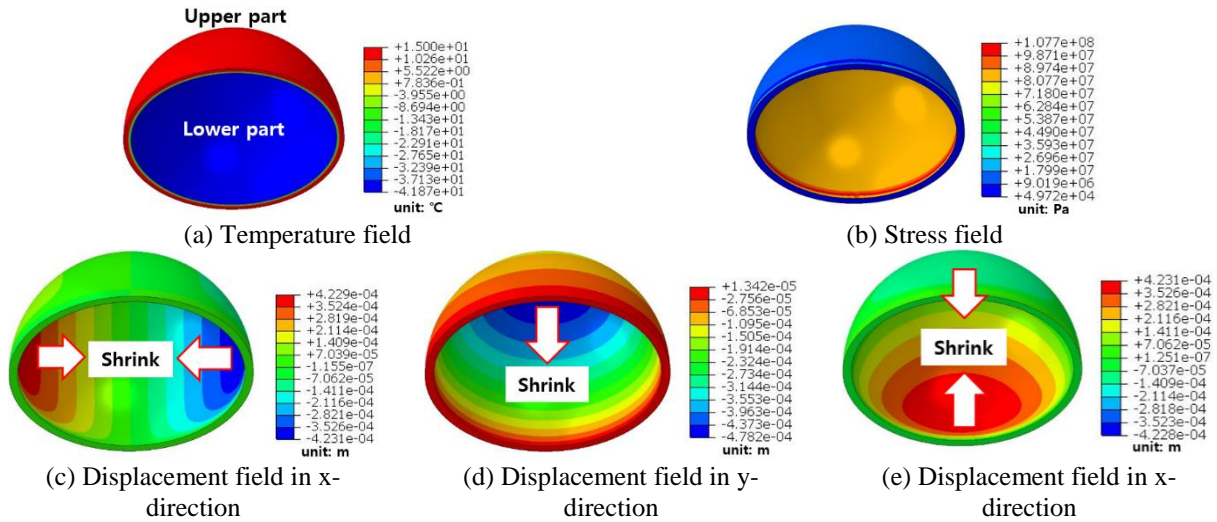


Figure 16: Results of the thermal-structural coupled analysis for the common bulkhead structure without any imperfections

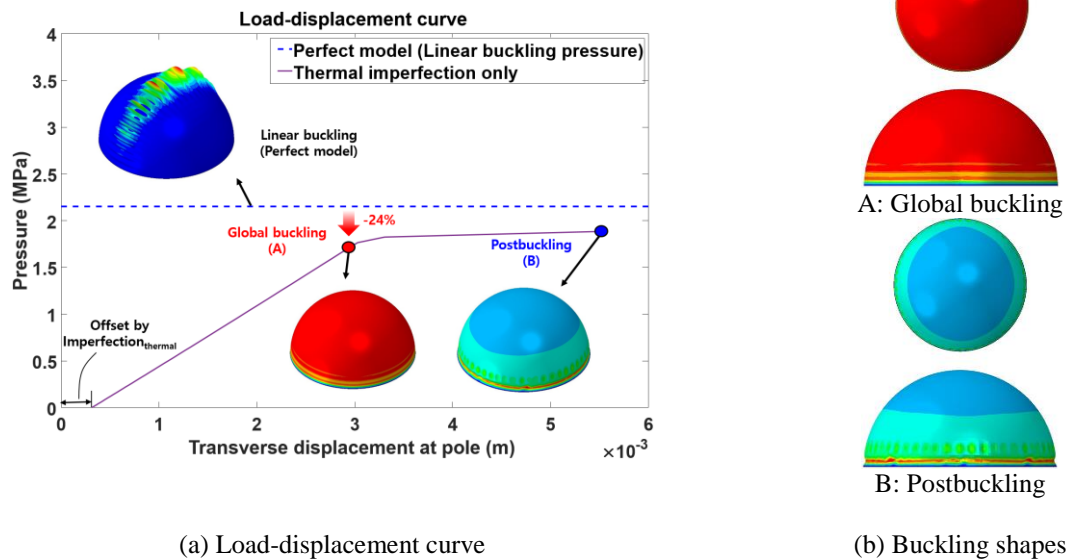


Figure 17: Postbuckling analysis results for the common bulkhead structure with thermal imperfection only

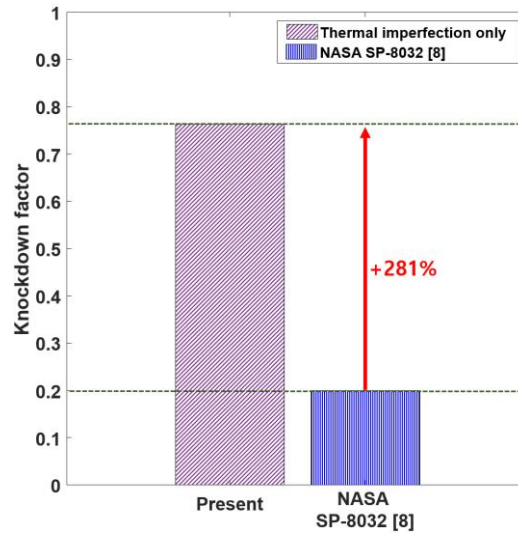


Figure 18: Comparison the buckling KDFs between the common bulkhead structure with thermal imperfection only and NASA's buckling design criteria [8]

3.4 Both geometric initial imperfection and thermal imperfection

Finally, this section considers both the geometric initial imperfection by the SPDA and the thermal imperfection from the thermal-structural coupled analysis for postbuckling analyses of the common bulkhead structure under external pressure. A transient thermal-structural coupled analysis is conducted to obtain the thermal imperfection for the deformed common bulkhead structures by SPDA application at $\mu_{\text{converged}} = 0.7$, as shown in Section 3.2 (Figure 13). As shown in Figure 19, the shrinkage of the common bulkhead structure is caused by a temperature decrease with temperature heat convection, which is similar to the results in Section 3.3.

Figure 20 illustrates the nonlinear postbuckling analyses when considering both $\text{Imperfection}_{\text{SPDA}}$ and $\text{Imperfection}_{\text{thermal}}$. As shown in Figure 20(a), the initial transverse displacement at the pole is represented as 0.053 m, generated from both the geometric initial imperfection and thermal imperfection, which is similar to the result in Section 3.2, but with a larger value. The deformed configurations for global buckling and postbuckling are shown in Figure 20(b). Global buckling (A) occurred with a dimple near the pole where the SPDA is applied. $\text{Imperfection}_{\text{SPDA}}$ and $\text{Imperfection}_{\text{thermal}}$ decreased the global buckling pressure by 1.002 MPa ($(N_{\text{cr}})_{\text{imperfect}}$), that is, by 53% compared to the $(N_{\text{cr}})_{\text{perfect}}$. In the post-buckling (B) state, the buckling waves grow in all directions. The buckling KDF considering both the geometric initial imperfection and thermal imperfection (0.465) in this section is 132% higher than that of NASA SP-8032 (0.200), as shown in Figure 21.

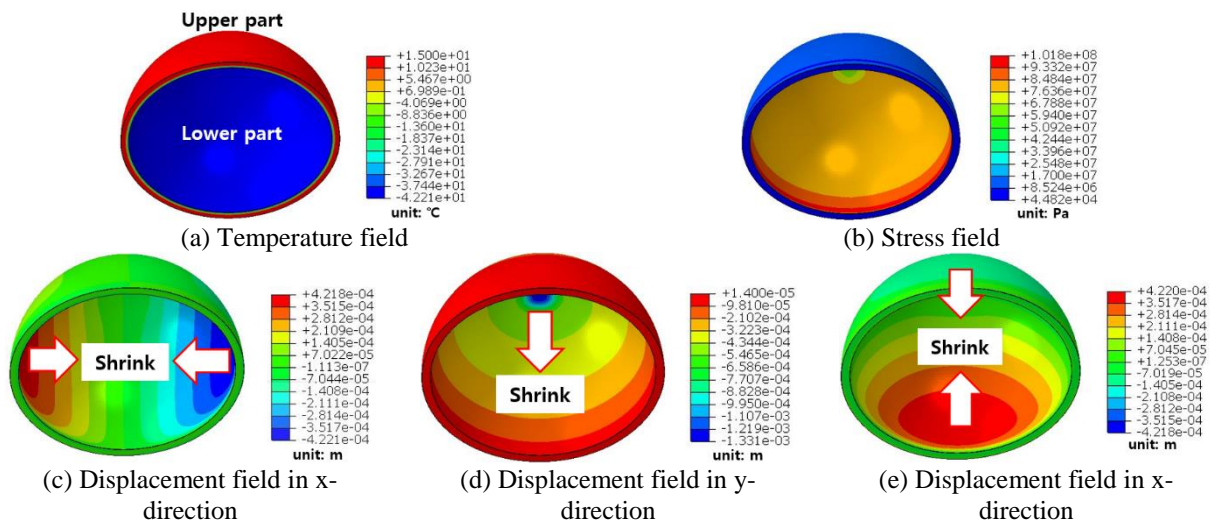


Figure 19: Results of the thermal-structural coupled analysis for the common bulkhead structure with geometric initial imperfection ($\mu_{\text{converged}} = 0.7$)

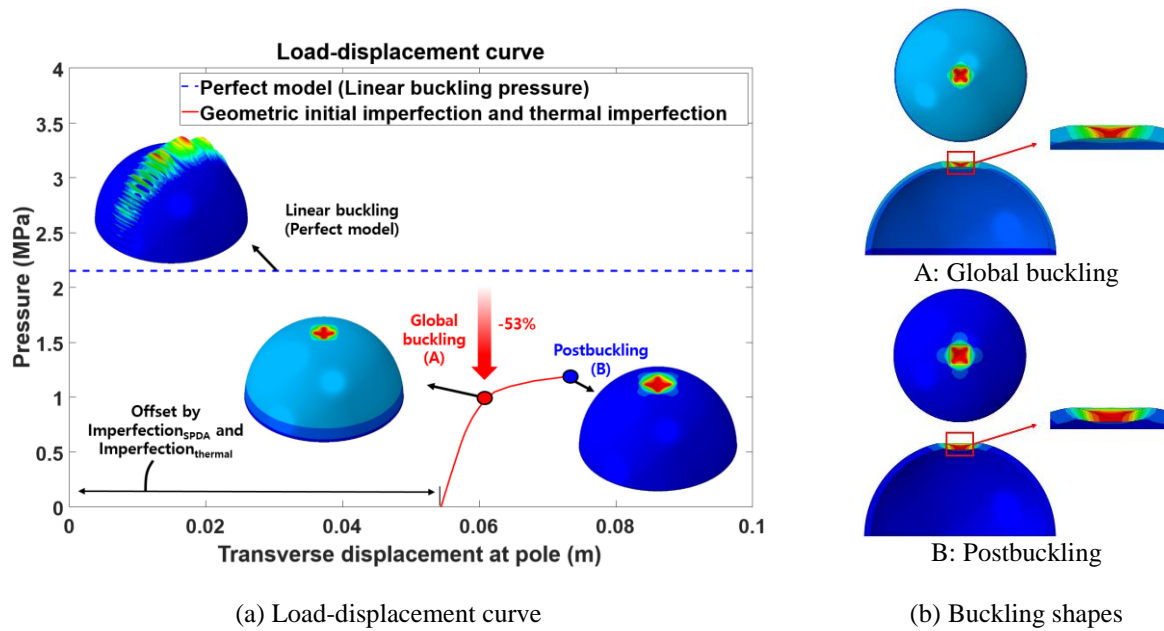


Figure 20: Postbuckling analysis results for the common bulkhead structure considering both the geometric initial imperfection and thermal imperfection

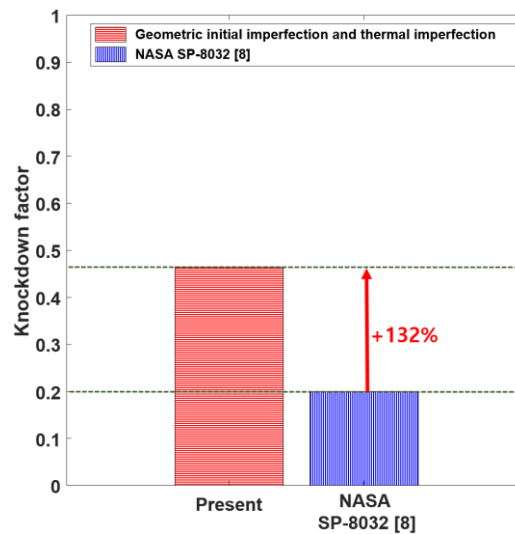


Figure 21: Comparison the buckling KDFs between the common bulkhead structure with both geometric initial imperfection and thermal imperfection, and NASA's buckling design criteria [8]

3.5 Comparison for the Knockdown Factors

The various buckling KDFs derived in this study are discussed in this section. Figure 22 shows a comparison of the buckling KDFs in this study and the NASA SP-8032. First, the geometric initial imperfection causes a significant reduction in the buckling KDF (0.512) for a common bulkhead structure; however, this is not the most conservative result in this study. Second, the buckling KDF with only thermal imperfection (0.763) exhibits a relatively high value. This is because the magnitude of the thermal imperfection is smaller than that of the geometric initial imperfection when the global buckling pressure converged. Finally, considering both the geometric initial imperfection and thermal imperfection decrease the buckling KDF (0.465) by 9% than that of the geometric initial imperfection only (0.512), not only the geometric initial imperfection but also the thermal imperfection should be considered when designing common bulkhead structures for space launch vehicles. The buckling KDF considering both the geometric initial imperfection and thermal imperfection (0.465) is the most conservative result in the present work; however, this is

132% higher than NASA's buckling design criteria. Therefore, when the present buckling KDF is applied to the design of a common bulkhead structure of space-launch vehicles, a lightweight design is possible.

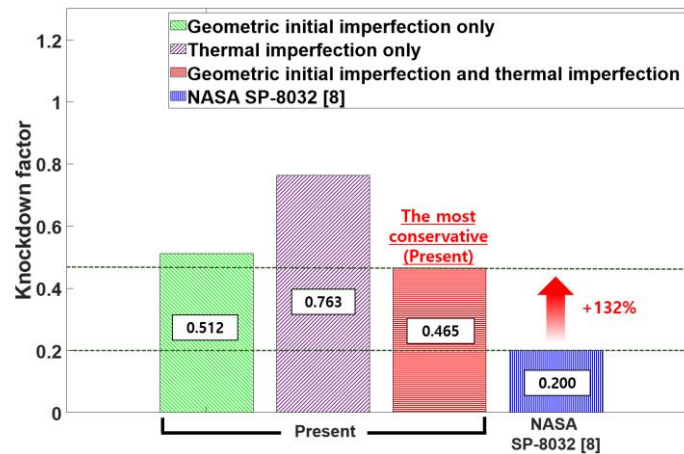


Figure 22: Comparison the present buckling KDFs and NASA's buckling design criteria [8]

4. Conclusion

In this study, common bulkhead structures for space launch vehicles were modeled as hemispherical shell structures with a foam core using the ABAQUS software. Post-buckling analyses using the quasi-static method were performed to derive the buckling KDFs for common bulkhead structures under external pressure. The geometric initial imperfections by SPDA were implemented as a dimple shape at the pole of the common bulkhead structures, and the thermal-structural coupled analyses generated thermal imperfection. The buckling KDFs considering only geometric initial imperfection (0.512) and thermal imperfection (0.763) were 156% and 281% higher than NASA's buckling design criteria (0.200), respectively. The buckling KDF with both geometric initial imperfection and thermal imperfection (0.465) was the most conservative result in this study, which was 132% higher than that of NASA SP-8032 (0.200). These results showed that both geometric initial imperfection and thermal imperfection should be considered for the safe design of common bulkhead structures, and lightweight design of space launch vehicles may be possible using the present buckling KDFs for common bulkhead structures.

Hemispherical common bulkhead structures were investigated in this study; however, various common bulkhead shapes, such as elliptical and torispherical shell structures, can be considered in future work.

References

- [1] Salt, D. J. 2010. Space operations for a new space era. In: *SpaceOps 2010 Conference Delivering on the Dream Hosted by NASA Marshall Space Flight Center and Organized by AIAA*. 1972.
- [2] Regab, M. M., Cheatwood, F. M., Hughes, S. J., and Lowry, A. 2015. Launch vehicle recovery and reuse. In: *AIAA SPACE 2015 Conference and Exposition*. 4490.
- [3] Mirshams, M., Naseh, H., and Fazeley, H. R. 2014. Multi-objective multidisciplinary design of space launch system using holistic concurrent design. *Aerospace Science and Technology*. 33(1): 40-54.
- [4] Updated May 01, 2017. Space launch report: SpaceX falcon data sheet.
- [5] Szelinski, B., Lange, H., Rottger, C., Sacher, H., Weiland, S., and Zell, D. 2012. Development of an innovative sandwich common bulkhead for cryogenic upper stage propellant tank. *Astronautica*. 81(1): 200-213.
- [6] Logsdon, T. 1997. *Orbital mechanics : theory and applications*. John Wiley and Sons.
- [7] Zhang, J., Zhang, M., Tang, W., Wang, W., and Wang, M. 2017. Buckling of spherical shells subjected to external pressure: a comparison of experimental and theoretical data. *Thin-Walled Structures*. 111: 58-64.
- [8] Weingarten, V. I. and Seide, P. 1969. Buckling of thin-walled doubly curved shells. NASA SP-8032.
- [9] Wagner, H. N. R., Hühne, C., and Niemann, S. 2018. Robust knockdown factors for the design of spherical shells under external pressure: Development and validation. *International Journal of Mechanical Sciences*. 141: 58-77.
- [10] Wagner, H. N. R., Hühne, C., Zhang, J., Tang, W., and Khakimova, R. 2019. Geometric imperfection and lower-bound analysis of spherical shells under external pressure. *Thin-Walled Structures*. 143: 106195.

- [11] Wagner, H. N. R., Hühne, C., Zhang, J., and Tang, W. 2020. On the imperfection sensitivity and design of spherical domes under external pressure. *International Journal of Pressure Vessels and Piping*. 179: 104015.
- [12] Wang, Y., Tang, W., Zhang, J., Zhang, S., and Chen, Y. 2019. Buckling of imperfect spherical caps with fixed boundary under uniform external pressure. *Marine Structures*. 65: 1-11.
- [13] He, J., Li, S., and Wang, S. 2018. Deformation behavior of sandwich hemispherical structure under axial compression at low temperature. *Composite Structures*. 203: 267-277.
- [14] Wang, S., Li, S., and He, J. 2017. Buckling behavior of sandwich hemispherical structure considering deformation modes under axial compression. *Composite Structures*. 163: 312-314.
- [15] Li, K., Wu, Z., Liu, M., Xu, X., and Xu, W. 2020. An application of reinforced polyurethane foam in design of the common bulkhead for cryogenic tanks. *Materials Science Forum*. 975: 182-187.
- [16] Grayson, G., Lopez, A., Chandler, F., Hastings, L., and Tucker, S. 2006. Cryogenic tank modeling for the Saturn AS-203 experiment. In: *42nd AIAA/ASME/SAE/ASEE Joint Propulsion Conference and Exhibit*. 5258.
- [17] Sumith, S., and Kumar, R. R. 2022. Thermo-structural analysis of cryogenic tanks with common bulkhead configuration. *Proceedings of The Institution of Mechanical Engineers, Part G: Journal of Aerospace Engineering*. 236: 900-909.
- [18] Darvizeh, M., Darvizeh, A., Shaterzadeh, A. R., and Ansari, R. 2010. Thermal buckling of spherical shells with cut-out. *Journal of Thermal Stresses*. 33: 441-458.
- [19] Wang, P., Lei, Y., and Yue, Z. 2013. Experimental and numerical evaluation of the flexural properties of stitched foam core sandwich structure. *Composite Structures*. 100: 243-248.
- [20] Choi, J. W., Choi, D. K., Roh, J. J., Lee, G. H., Lee, S. Y., and Roh, J. H. 2021. A study of bulkhead design in common bulkhead propellant tank considering transient heat transfer. In: *Proceeding of The Korean Society for Aeronautical and Space Sciences Fall Conference*.
- [21] Boccaccio, A., Casavola, C., Lamberti, L., and Pappalettere, C. 2013. Structural response of polyethylene foam-based sandwich panels subjected to edgewise compression. *Materials*. 6(10): 4545-4564.
- [22] Dewan, M. W., Huggett, D. J., Liao, T. W., Wahab, M. A., and Okeil, A. M. 2016. Prediction of tensile strength of friction stir weld joints with Adaptive Neuro-Fuzzy Inference System (ANFIS) and neural network. *Materials and Design*. 92: 288-299.
- [23] Badkul, A., Saxena, S., and Mondal, D. P. 2020. A numerical solution to accurately predict deformation behaviour of metallic foam material up-to densification region for the possible use in composite structures. *Composite Structures*. 246: 112419.
- [24] Amorim, J., and Pitarresi, G. 2010. Investigation on the indentation behavior of sandwich beams using crushable and hyperelastic foam cores. *EPJ Web of Conferences*. 6: 24002.
- [25] Carranza, I., Crocombe, A. D., Mohagheghian, I., Smith, P. A., Sordon, A., Meeks, G., and Santoni, C. 2019. Characterising and modeling the mechanical behaviour of polymeric foams under complex loading. *Journal of Material Science*. 54: 11328-11344.
- [26] Flores-Johnson, E. A., and Li, Q. M. 2010. Indentation into polymeric foams. *International Journal of Solids and Structures*. 47: 1987-1995.
- [27] Yoon, K. J., Kim, C. K., and Park, H. C. 2002. Nonlinear flexural deflection of thermoplastic foam core sandwich beam. *Journal of Composite Materials*. 36(13): 1529-1539.
- [28] Berger, L., Morgenthaler, M., Cantwell, M., Feichtinger, K., and Elkin, R. 2005. Dependence of sandwich damage initiation and crack propagation on core material fracture properties. In: *Proceedings of the 7th International Conference on Sandwich Structures*. 433-440.
- [29] Hühne, C., Rolfes, R., Breitbach, E., and Teßmer, J. 2008. Robust design of composite cylindrical shells under axial compression — simulation and validation. *Thin-Walled Structures*. 46: 947-962.
- [30] Kim, D. Y., Sim, C. H., Park, J. S., Yoo, J. T., Yoon, Y. H., and Lee, K. 2021. Buckling knockdown factors of composite cylinders under both compression and internal pressure. *Aerospace*. 8(11): 346.
- [31] Sim, C. H., Lee, C. M., and Park, J. S. 2022. Derivation of buckling knockdown factors using single perturbation load approach for hemispherical shell structures of launch vehicles. In: *Proceeding of The Korean Society for Aeronautical and Space Sciences Spring Conference*.
- [32] Sim, C. H., Lee, C. M., and Park, J. S. 2022. Derivation of knockdown factors for hemispherical shell structures with foam core. In: *Proceeding of The Korean Society for Aeronautical and Space Sciences Fall Conference*.
- [33] Lee, C. M., Sim, C. H., and Park, J. S. 2023. Thermal insulation performance comparison using boil-off mass and boil-off rate for common bulkhead structures of space launch vehicles. *Journal of the Korean Society for Aeronautical and Space Sciences*. 51: 227-234.
- [34] Yousefi, M., and Ghalehnavi, M. 2018. Finite element model for interlayer behavior of double skin steel-concrete-steel sandwich structure with corrugated-strip shear connectors. *Steel and Composite Structures*. 27(1): 123-133.